ADVANCED FUNCTIONAL MATERIALS
www.afm-journal.de

Highly Deformable Phototunable Viscoelastic Fluid Interface Modulates Cellular Adaptive Wetting Behavior

*Junhong Zhou, Hongxin Wang, and Jun Nakanishi**

Emerging evidence shows that the viscoelastic cues of the e Ixtracellular matrix (ECM) regulate cellular functions and fates. However, as cells are viscoelastic, force dissipation occurs within themselves as well as the ECM side, implying the existence of reciprocal viscous regulation between the two. Here, a fluid-based scaffold with tunable viscoelasticity has been developed to investigate its impact on the cell adhesion process. The platform is based on the water–perfluorocarbon interface decorated with diacetylene-based phospholipid membranes (IPLMs), whose viscoelasticity can be systematically manipulated by photocrosslinking. Further introduction of a cell-adhesive peptide and fluorescent tag allows cell adhesion at the highly deformable fluid interface and confocal observation of dynamic cell–model ECM interactions. The viscoelasticity-tunability is confirmed by fluorescence recovery after photobleaching, interfacial rheology, and atomic force microscopy nanoindentation. Cells seeded at the IPLM exhibit so-called adaptive wetting, where the interface first deforms toward the out-of-plane direction before cellular dimensional changes, followed by cellular flattening and interfacial restoration. Furthermore, the quantification of these parameters reveals a biphasic response against the crosslinking levels, which indicates that the cell-ECM viscosity balance determines adaptive wetting phenotypes. The platform may enable the prediction of dynamic adhesion responses in physiological and pathological processes.

1. Introduction

In natural tissues, cells reside in a highly dynamic extracellular matrix (ECM), whose composition and mechanics change during development and disease progression. Biomaterials with mechanical and biochemical cues can be customized to modulate cellular behaviors.[1] Synthetic elastic substrates with varying stiffness induce various mechanobiological processes, including cellular adhesion behavior, cytoskeletal contractility, and stem cell fate decisions.[2] Since many soft tissues are not purely elastic, rather than that they exhibit a viscoelastic nature with time-dependent mechanical responses.[3] The combination of the elastic and viscous properties is important for regulating cellular activities.

Recently, the role of substrate stress relaxation (viscous behavior) in cell mechanotransduction was revealed through the manipulation of the bulk viscoelastic properties of hydrogels.[4] It is reported that viscoelastic hydrogels with the appropriate stress relaxation promote the spreading and differentiation of mesenchymal stem cells (MSCs).[5] The tuning of viscous components in biomaterials can also be achieved by engineering molecular adsorption, ligand tethering, or ligand diffusivity of a solid-supported substrate.[6] To highlight the viscous component, supported lipid bilayers (SLBs) have been utilized to control RGD (Arg–Gly–Asp) ligand mobility depending on the lipid compositions, which allows us to understand the impact of interfacial viscosity on cell adhesion behaviors.[7] Dissipation occurs in either the materials' bulk or interface, and the viscous nature regulates the cellular spreading speed in the framework of the molecular clutch scenario in a similar fashion to the elastic component.[8] However, the forces generated by the actin retrograde flow are applied not only to the extracellular matrices but also to the cellular interior.[9] By considering that cells also have viscoelastic responses,[10] force dissipation can be expected within the cells, altering cellular adhesion dynamics, including cellular morphological changes and dimensional transitions.

J. Zhou, H. Wang, J. Nakanishi
Research Center for Macromolecules and Biomaterials
National Institute for Materials Science (NIMS)
1-1 Namiki, Tsukuba, Ibaraki 305-0044, Japan
E-mail: NAKANISHI.Jun@nims.go.jp

The ORCID identification number(s) for the author(s) of this article can be found under https://doi.org/10.1002/adfm.202414534

© 2025 The Author(s). Advanced Functional Materials published by Wiley-VCH GmbH. This is an open access article under the terms of the Creative Commons Attribution License, which permits use, distribution and reproduction in any medium, provided the original work is properly cited.

DOI: 10.1002/adfm.202414534

J. Zhou, J. Nakanishi
Graduate School of Advanced Science and Engineering
Waseda University
3-4-1 Okubo, Shinjuku-ku, Tokyo 169-8555, Japan

J. Nakanishi
Graduate School of Advanced Engineering
Tokyo University of Science
6-3-1 Niijuku, Katsushika-ku, Tokyo 125-8585, Japan

16163028, 0, Downloaded from https://advanced.onlinelibrary.wiley.com/doi/10.1002/adfm.202414534 by Cochrane Japan, Wiley Online Library on [16/01/2025]. See the Terms and Conditions (https://onlinelibrary.wiley.com/terms-and-conditions) on Wiley Online Library for rules of use; OA articles are governed by the applicable Creative Commons License

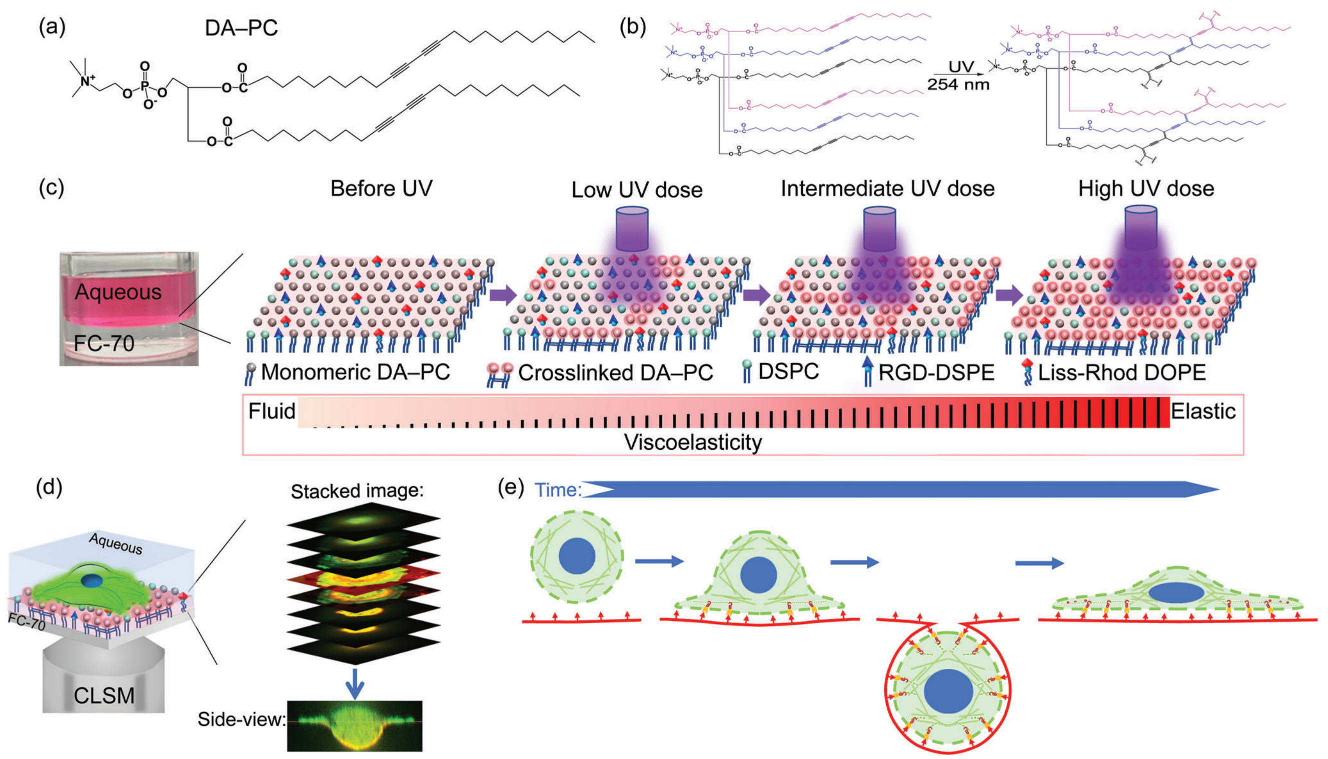

Figure 1. Emergence of cellular adaptive wetting behaviors at highly deformable fluid interfacial phospholipid membranes (IPLMs) depending on photo-tuned interfacial viscoelasticity. a) Chemical structure of the monomeric photocrosslinkable phospholipid (DA–PC). b) UV-induced polymerization reaction of DA–PC molecules. c) The crosslinked DA–PC acting as physical barriers within IPLM to alter the viscoelastic nature of the water–PFCL (FC-70) interface depending on UV dose. The head groups of monomeric and crosslinked DA–PC are shown in gray and pink, respectively. The lipid membranes also contain DSPC (cyan), cell-adhesive RGD-DSPE (blue), and fluorescent Liss-Rhod DOPE (red). The color bar increments shown below represent the viscoelasticity changes. d) Confocal microscopic observation and image reconstitution strategy of the side view from the stacked images of cells (green) and IPLM (red). e) Schematic drawing of cellular adaptive wetting, where the interface deformed first without cellular flattening, followed by cellular spreading and interfacial restoration. Green, actin. Red, IPLM with RGD ligand. Blue, nucleus. Yellow, integrin. Dark red, focal adhesion.

Our group has recently reported a new platform that can highlight the impact of cellular viscoelastic nature on spreading behaviors.[11] The platform is based on water–perfluorocarbon liquid (PFCL) interfaces decorated with phospholipid membranes (IPLMs), containing a cell-adhesive peptide ligand and fluorescent tag. The bioinert nature of the phospholipid layer prevents protein adsorption and robust protein nanofilm formation at the interface, maintaining the intrinsically super-soft nature of the fluid interface. On this extremely high deformable IPLM toward the out-of-plane direction, the cells exhibit a unique adaptive wetting behavior, in which the interface deforms before cellular dimension changes, followed by interfacial restoration and cell flattening. The cellular adaptive wetting behavior is clearly detectable because the cell traction-mediated IPLM deformation speed is faster than that of cytoskeletal rearrangement, thereby reflecting the cellular viscoelastic nature. In fact, we have demonstrated that cellular adaptive wetting can be simulated by the wetting of viscoelastic polymeric liquid drops at air–water interfaces.[11] By considering the significant role of ECM viscoelasticity in cell spreading in general, it is reasonable to assume that cellular adaptive wetting can also depend on ECM viscoelasticity. However, our previous platform was not suitable to systematically address this issue.

In this study, we refined the previous IPLM system to investigate how dynamic viscoelasticity on cell-ECM interactions affects cellular adaptive wetting behavior. Our updated platform integrates diacetylenyl phosphatidylcholine (DA–PC) with other lipid species that self-assembled at the water–PFCL interface (**Figure** 1a). DA–PC with triple bonds was covalently crosslinked with neighboring DA–PC molecules by 254 nm ultraviolet (UV) light irradiation (Figure 1b). This was utilized to control the degree of crosslinking depending on the UV dose in SLBs, changing the speed of mass transport along the membranes by the formation of stationary obstacles.[12] Therefore, we hypothesized that DA–PC lipids were suitable for controlling the viscosity of assembled phospholipid membranes to manipulate the overall viscoelastic properties of super-soft DA–PC-based IPLM systems (Figure 1c). Confocal analysis of the IPLM, together with a reconstituted cellular side view from the stacked images, allowed us to investigate the impact of viscoelasticity on cell-IPLM interactions (Figure 1d). The cellular adaptive wetting behavior was observed (Figure 1e), where the interface deformed first without cellular flattening, followed by cellular spreading and interfacial restoration. This clearly demonstrated the potential of this platform in studying cellular adhesion behaviors with a mutually adaptive nature for both ECM and cells.

© 2025 The Author(s). Advanced Functional Materials published by Wiley-VCH GmbH

16163028, 0, Downloaded from https://advanced.onlinelibrary.wiley.com/doi/10.1002/adfm.202414534 by Cochrane Japan, Wiley Online Library on [16/01/2025]. See the Terms and Conditions (https://onlinelibrary.wiley.com/terms-and-conditions) on Wiley Online Library for rules of use; OA articles are governed by the applicable Creative Commons License

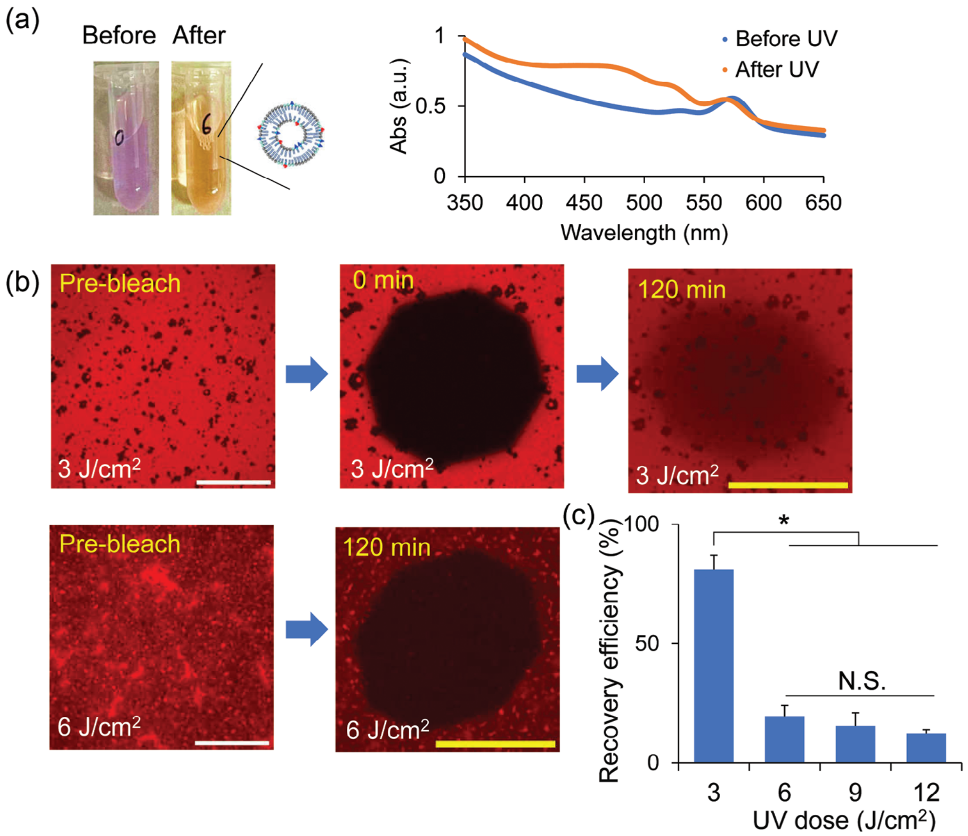

Figure 2. Photocrosslinking reaction of DA–PC within the vesicles and fluid interface. a) Photographic images (left) and UV–vis absorption spectrum (right) of lipid vesicles before and after 254-nm UV irradiation for 6 J cm^{-2}. b) Evaluation of the fluid nature of IPLM by fluorescence recovery after photobleaching (FRAP) with irradiation of 545 ± 5 nm light at a polygonal region. Fluorescence images represent the same area before photobleaching (pre-bleach), or after 0- and 120-min intervals from photobleaching. Red color represents rhodamine-labeled lipid. Scale bars represent 50 µm. c) Quantitative analysis of the recovery efficiency in the FRAP experiment shown in (b) and Figure S3 (Supporting Information). The fluorescence intensity (F.I.) values in the bleached regions were normalized to the value before photobleaching. The number of experiments was three for each case. Statistical differences were analyzed using Student's *t*-test: $^{*}p < 0.05$. N.S., no significance, $p \geq 0.05$.

2. Results

2.1. Modulation of Interfacial Phospholipid Membrane Viscosity Via UV Dose

In this study, photocrosslinkable IPLM was prepared by coating the water–PFCL interface with phospholipid membranes via vesicle fusion (Figure S1, Supporting Information). We first studied the photocrosslinkable nature of the phospholipid vesicles containing DA–PC before and after their assembly at the water–PFCL interface. The composition of vesicles is critical for the efficient control of membrane viscosity depending on the degree of cross-linking.[13–16] Here, we used DA–PC:distearoylphosphatidylcholine (DSPC):lissamine rhodamine-labeled dioleoylphosphatidylethanolamine (Liss–Rhod DOPE) = 85/14.5/0.5 mol.%. Within this lipid composition, the saturated DSPC species enable the DA–PC molecules to pack tightly together to improve the crosslinking efficiency.[13] The Liss–Rhod tag was introduced for the following fluorescence observation of lipid distribution as well as the evaluation of the viscous nature of the fused membranes by fluorescence recovery after photobleaching (FRAP) experiments.

Crosslinking of vesicles containing the DA–PC molecule was studied by UV–visible (vis) spectroscopy. **Figure 2a** shows the photos and the absorption spectra of the phospholipid vesicles dispersed in PBS buffer before and after UV irradiation at 254 nm. The significant change in the solution color and increase in the absorbance of the wavelength less than 550 nm indicated the UV-triggered polymerization of DA–PC.[13] Two new peaks emerged around 480 and 525 nm. It is known that the absorption peak wavelength depends on the polymer units; the more coupled the polymer units, the longer the absorbance peak wavelength. Accordingly, the absorption peaks around 480 and 525 nm corresponded to shorter and longer polymerized units, respectively.[17,18] We did not further investigate the correlation between the magnitude of the two absorbance peaks and the increase in the UV dose for the vesicles because of the difference in curvature between the vesicles and the planar IPLM. This follows the opinion that planar surfaces may have larger well-packed domains than curved vesicles, changing the crosslinking efficiency.[19]

Next, we evaluated UV-induced crosslinking at the water–PFCL interface in terms of the distribution of the Liss–Rhod-labeled fluorophore. Phospholipid molecules with an

© 2025 The Author(s). Advanced Functional Materials published by Wiley-VCH GmbH

amphiphilic structure in the vesicles self-assembled into a continuous planar surface at the water–PFCL interface prior to UV irradiation (Figure S1c, Supporting Information). Despite the complexity of the lipid composition, we expected all the lipid components, regardless of their phase transition temperature, to transfer to the planar phospholipid membrane at ambient temperature. This is because according to the literature,[20] the planar lipid layer can be formed by supplying a sufficient amount of vesicles in aqueous phase to ensure efficient mass transfer from the vesicles to the surface. In our case, bulk aqueous dispersion also allowed efficient mass transfer of phospholipids to the interface compared with the assembled thin IPLM layer. After the given time for assembly, the Liss–Rhod fluorophore was homogenously distributed in the membrane without UV irradiation (Figure S1d, Supporting Information). To assess the morphology of the interface and presence of polymerized DA–PC in the IPLM, atomic force microscopy (AFM) was performed. Topography images of IPLM after treatment with 3, 6, 9, and 12 J cm^{-2} UV doses are shown in Figure S2 (Supporting Information). The roughness of the resulting polymerized IPLM decreased gradually with increasing UV dose. This follows the opinion that during polymerization the diacetylene lipid layer shrinks in the vertical direction.[21]

It is known that the polymerization of lipid layers composed of polymerizable and nonpolymerizable lipids can cause the polymerized domains to grow through the diffusion of reactive DA–PC monomers.[22] Therefore, obvious phase separation was expected depending on the UV dose. Here, the distribution of lipids within the IPLM was investigated by fluorescence microscopy. Figure S3 (Supporting Information) (pre-bleach part) represents the changes in the distribution of the Liss–Rhod fluorophores depending on UV dose. At a low UV dose, such as 3 J cm^{-2}, small black dots representing polymerized DA–PC-rich clusters appeared across the membrane surface through separation from the mixture of fluorophore lipids and the uncrosslinked monomer DA–PC, showing the majority with red fluorescence. In addition, large red fluorescent regions that shared a similar fluorescence featuring with the original IPLM before UV irradiation (Figure S1d, Supporting Information) indicated the capability for further crosslinking of DA–PC. At higher irradiation energies of 6 and 9 J cm^{-2}, the polymerized regions were connected to each other to make the black domain predominant on the surface, with the Liss–Rhod fluorophore confined within smaller fluorescent dot regions, indicating that polymerized domains grew gradually via the incorporation of reactive DA–PC monomers.[23] When the irradiation energy increased to 12 J cm^{-2}, the crosslinked DA–PC molecule ratio became much larger, and the surface was mostly covered by the black domains with enlarged fluorescent regions in smear-like structures due to the stronger phase separation between the two domains. Therefore, the growth of polymerized domains was promoted by increasing the UV dose.

We then investigated the viscosity of the DA–PC-based IPLM at the water–PFCL interface upon UV irradiation of the planar surface, as polymeric domains would serve as obstacles hindering the lateral diffusion of fluid lipids (Figure 2b).[12] The lateral diffusivity of the fluorescein-labeled phospholipid membrane was measured by FRAP, which is also a critical characteristic of the viscosity of the IPLM based on the molecule diffusion because the inertia of a liquid and its softness make the conventional characterization of viscosity a challenging task.[24] Using this method, a defined polygon was selected as a region of interest (ROI), and subsequently, the fluorophore was initially bleached by exposing strong light at the ROI. Time-lapse fluorescence microscopy images showed bleaching retention or recovery of fluorescence in the bleached region of the entire membrane depending on the diffusion of the fluorescent molecules from the surrounding, which correlated with the different crosslinking levels of the membranes.

When the irradiation energy was 3 J cm^{-2}, there was a slight drift in the entire membrane, and the intensity of the bleached area recovered to 80% of the original value after bleaching for 2 h (Figure 2c). As low UV dose was supposed to only produce small dark polymerized islands, they were not able to cover entire regions of the membranes (Figure 2b and 3 J cm^{-2} case). Thus, the entire IPLM was mobile at room temperature (RT), which enabled fluorophore recovery in the bleached region. Therefore, the rapid lateral diffusion of fluorescent molecules from the surroundings for the recovery indicated that the IPLM had lower viscosity, because of insufficient irradiation. Thereafter, upon increasing the UV dose in the range of 6 to 12 J cm^{-2}, there was almost no drift of the membrane because the large, crosslinked DA–PC regions had an oriented structure in the gel phase, which prevented the entire mobility. It should be noted that there was little recovery of intensity in the bleached areas starting from 6 J cm^{-2} (Figure S3, Supporting Information, 120 min part), as the entanglement of polymer clusters acted as a barrier to block lateral diffusion of fluid lipids. From the dose-dependency of the percentage of the fluorescence recovery in the bleached regions (Figure 2c), there was a drastic change in the fluorescence recovery from 3 to 6 J cm^{-2}. However, this did not mean the completion of the crosslinking reaction above 6 J cm^{-2}, rather it continued to change the viscoelastic nature with prolonged irradiation. In fact, interfacial rheology with double wall ring (DWR) geometry showed the change in the crossover points of G′ and G″ toward a lower frequency (Figure S4, Supporting Information), which demonstrated continuous alteration of the viscoelastic nature through increasing crosslinking levels.[25,26]

2.2. Characterization of IPLM Mechanical Tunability by Atomic Force Microscopy (AFM)

As discussed, the extensively polymerized domains of DA–PC resulted in the fluid–gel transition and significantly lowered lipid diffusion, which reflected the increases in interfacial viscosity in the lateral direction. Simultaneously, the conjugated backbone in the gel phase conferred high elasticity to the membrane in the vertical direction. Next, we investigated the impact of the crosslinking level on the mechanical properties of the IPLM using AFM nanoindentation to measure the apparent modulus at the liquid–liquid interface by using a colloidal probe with a 300 nm radius (**Figure 3a**).

The nanoindentation mode allowed us to obtain force-distance curves on the whole 5 × 5 µm^2 scan with a resolution of 64 pixels × 64 pixels. Figure 3b shows a representative force-distance curve as an example from the below stiffness map (Figure 3d, each map = 4 × 4 = 16 force curves). By fitting each force curve with the

© 2025 The Author(s). Advanced Functional Materials published by Wiley-VCH GmbH

16163028, 0, Downloaded from https://advanced.onlinelibrary.wiley.com/doi/10.1002/adfm.202414534 by Cochrane Japan, Wiley Online Library on [16/01/2025]. See the Terms and Conditions (https://onlinelibrary.wiley.com/terms-and-conditions) on Wiley Online Library for rules of use; OA articles are governed by the applicable Creative Commons License

16163028, 0, Downloaded from https://advanced.onlinelibrary.wiley.com/doi/10.1002/adfm.202414534 by Cochrane Japan, Wiley Online Library on [16/01/2025]. See the Terms and Conditions (https://onlinelibrary.wiley.com/terms-and-conditions) on Wiley Online Library for rules of use; OA articles are governed by the applicable Creative Commons License

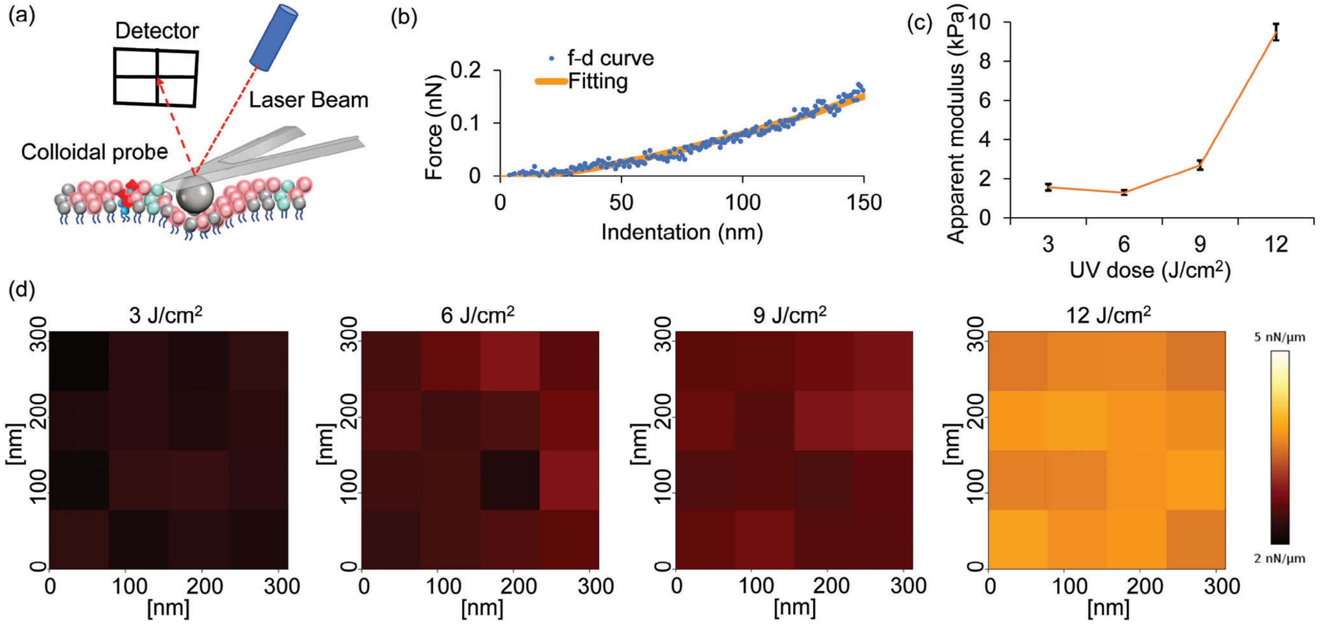

Figure 3. Mechanical property characterization of the UV-irradiated IPLMs by AFM nanoindentation. a) Scheme of AFM nanoindentation. b) Representative force-deformation curve (blue dotted line) and fitting curve based on the Hertz model (orange solid line) for the IPLM with 9 J cm^{-2} UV-irradiation. c) Dose-dependent changes in apparent modulus. Mean ± s.d. of the 16 different positions in d) are plotted. (d) AFM stiffness maps of the UV-irradiated IPLM in 300 × 300 nm^2 (4 pixels × 4 pixels).

Hertz model (Figure S5, Supporting Information) to obtain and plot the respective apparent modulus values, we determined how mechanical stiffness correlated with exposure to contrasting UV doses by varying the degree of DA–PC crosslinking. The result showed a dose-dependent increase in the stiffness of membranes above 6 J cm^{-2}, demonstrating the tunability of mechanical stiffness (Figure 3c). However, the apparent modulus of the IPLM did not increase linearly with the UV dose, presumably because the conjugation length of DA–PC molecules is not sufficiently high to alter the membrane stiffness with the short irradiation.

The apparent modulus given by AFM analysis reflects the state of the IPLM coated interface (the deformability), although it is composed of material modulus and interfacial tension, considering the different mechanics between interfacial and conventional bulk materials.[27] To understand the contribution of the above two factors to the IPLM mechanics for the minimum and maximum crosslinking level, we dismantled the interfacial tension at the fluid interface (pre-stress) and the IPLM crosslinking-derived modulus, based on the informatics-assisted AFM method developed by our group.[28] In Figure S6 (Supporting Information), the estimated moduli and the stress (derived from interfacial tension) are shown as red and blue plots, respectively. The results demonstrated these two values are comparable for 3 J cm^{-2}, whereas the contribution of materials' modulus is dominating for 12 J cm^{-2} due to the increased crosslinking levels. Therefore, we can say that the interfacial viscoelasticity changed from the interfacial tension-dominating state to the materials modulus-dominating one through increasing the crosslinking level.

Furthermore, by drawing the combination relationships between elasticity together with mobility and various UV doses (Figure S7, Supporting Information), the elasticity and mobility gradually increased and decreased, respectively. Particularly in the case of 6 J cm^{-2}, the elasticity did not increase significantly despite the generally decreased mobility. In this respect, the IPLM at 6 J cm^{-2} may be located close to the boundary between the fluid–gel transition. The FRAP experiment reflects the viscous nature of lipids in terms of molecular diffusion against Van der Waals interaction between the lipid molecules, whereas AFM nanoindentation reflects membrane mechanics against force exertion. Therefore, it is no wonder these two methods demonstrate different boundaries in the transition between the viscosity- to elasticity-dominant states. Upon 9 J cm^{-2} exposure, the IPLM transitioned to a more solid-like state; thus, there was an increase in the mechanics in a dose-dependent fashion. Therefore, mobility and mechanical experiments confirmed the phototunable viscous and elastic nature of the membranes. The non-mobile IPLM generated from 6 J cm^{-2} exposure displayed high viscosity, and the elasticity increase observed from 9 J cm^{-2} exposure via AFM nanoindentation originated from its solid-like nature in response to high crosslinking levels.

2.3. Impact of the Viscoelastic Nature of IPLM on Cellular Adaptive Wetting Characteristics

Our previous study defined adaptive wetting behavior with the attribution of out-of-plane deformation at the fluid interface and dynamic mechanical energy transfer in quasi-3D dimension.[11] Here, we applied the above-discussed customizable fluid interface to examine how IPLM viscoelasticity alters cellular adaptive wetting behaviors. Specifically, we investigated early-stage cellular adhesion behaviors after seeding Madin–Darby canine kidney (MDCK) cells stably expressing lifeact-green fluorescent protein (GFP) as these epithelial cells exhibit unique characteristics in

© 2025 The Author(s). Advanced Functional Materials published by Wiley-VCH GmbH

16163028, 0, Downloaded from https://advanced.onlinelibrary.wiley.com/doi/10.1002/adfm.202414534 by Cochrane Japan, Wiley Online Library on [16/01/2025]. See the Terms and Conditions (https://onlinelibrary.wiley.com/terms-and-conditions) on Wiley Online Library for rules of use; OA articles are governed by the applicable Creative Commons License

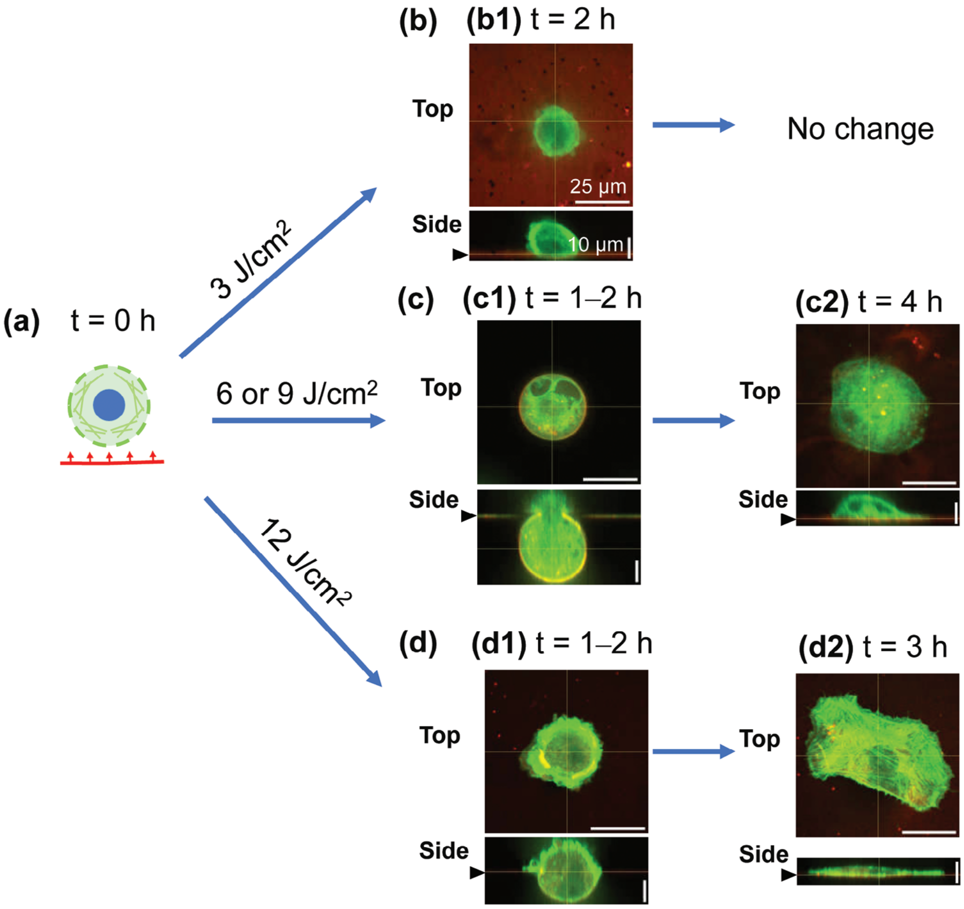

Figure 4. Representative images of cellular wetting behaviors at the IPLM with different UV doses. a) Cells are seeded to IPLMs with 3, 6, 9, or 12 J cm^{-2} irradiation. b–d) Time-dependent morphological transition and interfacial deformation. Green, lifeact-GFP. Red, rhodamine-labeled lipid. (b) Cells did not spread at 3 J cm^{-2} IPLM. (c,d) Cellular adaptive wetting with (c) deep and (d) shallow invasion, at 6 (or 9) and 12 J cm^{-2} IPLMs, respectively. The top views in each case are the cross-sectional images. The side views were reconstituted from stacked confocal images. Arrowheads on the left indicate the water–PFCL interface level.

the interactions between the cell sheets and substrate through a tug-of-war mechanism.[29,30] It is reasonable to assume that a single epithelial cell can also exert force in all directions considering that in vivo they are 3D and can sense and respond to the 3D geometry in their environment.[31]

First, the bioinertness of IPLM in preventing protein adsorption was investigated as it is critical to maintain the intrinsically super-soft nature of the fluid interface.[11] Compared with the pristine perfluorocarbon liquid, the headgroup of the IPLM derived from phospholipid molecules formed a hydration layer that largely prevented nonspecific protein adsorption regardless of the UV irradiation energy (Figure S8, Supporting Information). Therefore, the deformable nature of the fluid interface toward the out-of-plane direction can also be expected in our photocrosslinkable IPLM system. Next, the biocompatibility of the IPLM was assessed by evaluating cell survival using a live/dead staining assay after incubation of MDCK cells with the scaffolds for 2–3 h. As shown in Figure S9 (Supporting Information), the percentage of live cells (appeared as green fluorescence) was almost 100% for all the scaffolds, which verified the IPLM scaffolds had good biocompatibility.

Given that photocrosslinkable IPLM are bioinert and biocompatible, we next investigated the adhesion behaviors of the MDCK cells expressing lifeact-GFP thereon by confocal laser scanning microscopy (CLSM) (**Figure 4**). Considering the heterogeneous adhesion dynamics of individual cells owing to the mixed clones of cells expressing different levels of lifeact-GFP and unsynchronized cell cycles, we first analyzed cellular adaptive wetting processes of different cells at specific time points and looked at the impact of the viscoelastic properties of the IPLM. Figure 4 shows representative images of time-dependent behaviors. At lower crosslinking levels (3 J cm^{-2}), most cells were attached with almost no downward indentation throughout the observation time (Figure 4b1). In contrast, unique adaptive wetting behaviors were observed by increasing irradiation energy to more than 6 J cm^{-2}, in a fashion similar to our previous study,[11] where IPLM deformed first followed by interfacial restoration and cellular dimensional changes. Specifically for 6 and 9 J cm^{-2} irradiation, almost the entire cell body went below the original water–PFCL level at the invasion phase (Figure 4c1) but returned to almost the original level and spread after ≈4 h (Figure 4c2). This can be clearly observed

© 2025 The Author(s). Advanced Functional Materials published by Wiley-VCH GmbH

by focusing on the same cells (Figure S10, Supporting Information). When we further increased the irradiation energy to 12 J cm^{-2}, the invasion depth decreased and IPLM deformation was partially retained (Figure 4d1). Subsequently, the deformed IPLM transitioned from the PFCL phase to the aqueous phase and cells eventually showed a large-spreading morphology with IPLM restoration at the end (Figure 4d2). By considering FRAP and AFM nanoindentation experiments, the observed changes in IPLM deformation and cellular dimension for different irradiation energies can be attributed to the regulation of cellular (adaptive) wetting dynamics by the viscoelastic nature of IPLM.

To further check cellular morphology with a prolonged timescale, the observation was extended up to 15 h. Cells showed different dimensions and spreading morphology as if the cells were undergoing epithelial-mesenchymal transition (EMT) (Figure S11, Supporting Information). Like less viscous 6 J cm^{-2} IPLM, the cells showed the epithelial trait with partial spreading and maintained a larger cell dimension. In contrast, in the case of more viscous 9 and 12 J cm^{-2} IPLMs, the cells gained a mesenchymal morphology with a larger spreading area. It is known that cell morphology is correlated with cellular fate decision corresponding to the mechanical cues. Therefore, the interplay between cell and IPLM could be an indication of changes in cell functions.

2.4. Quantitative Analysis of the Impact of IPLM Viscoelastic Nature on Cellular Dimension and Interfacial Deformation during Adaptive Wetting

As discussed, the cells showed different wetting behaviors depending on the interfacial viscoelasticity, with different degrees of cellular invasion into the PFCL phase. However, the trends were only discussed by a representative profile on IPLM of each crosslinking level, and in fact, cellular wetting behaviors were different from one cell to another. To further understand the entire picture of cellular wetting behaviors for single-cell populations, we focused on and quantitatively evaluated cellular morphology during a specific time window (1–2 h after cell seeding), when cellular invasion into PFCL was largest for nearly all irradiation energies. To simplify this analysis, we first divided cell attachment phenotypes into two groups: either the invasion depth (d) was smaller than 2 µm ($d<2$) or larger ($d \geq 2$) (**Figure 5a**). This depth was chosen because two planes need to be separated at a certain distance to discuss cellular incident angle (θ) precisely. The former group was further divided into two based on the cellular appearance in the green fluorescence channel: i) no invasion and ii) highly spreading morphology (Figure 5b). By comparing D_0 and D_2 at the depth of 0 and 2 µm processed with the red fluorescence channel, which was the diameter of the convergent boundary between cell and IPLM at the cross-section image (Figure 5a), the latter group was also divided into two: iii) partial invasion with incident angle (θ) < 90°and iv) the deep invasion with θ > 90° (Figure 5b). For a partial invasion, there was a large opening at the water–PFCL interface with a protrusion structure at the cell periphery for partial cell body diving (Figure 5b,iii). In contrast, the deep invasion had a small opening at the level of the water–PFCL interface, where the entire cell body was almost wrapped by the IPLM, with a significant degree of deformation observed (Figure 5b,iv).

The histogram of single-cell populations involved in the four groups is plotted in Figure 5c. The quantification of the cell population in each morphology clearly represents the reproducible observation of cellular deep invasion (Figure 5b,iv) for 6 and 9 J cm^{-2}, that is, at least 30%–50% of the total number of cells. By considering the single-cell invasion process (Figure S10, Supporting Information) as well as the cellular heterogeneous nature, we cannot exclude the fact that there may be more cells than this population; as we fixed the observation time point at 1–2 h, some cells might have already finished diving or were about to go into the deep dive afterward. In contrast, most cells stayed at the shallow invasion (47%) (Figure 5b,iii) or spreading morphology (37%) (Figure 5b,ii) on the stiffest IPLM at a UV dose irradiation of 12 J cm^{-2}. In addition, the cells at the IPLM at a UV dose of 3 J cm^{-2} were mostly attached at the interface with no invasion (70%) (Figure 5b,i) or partial invasion (30%) (Figure 5b,iii). The higher population of deep invasion (iv) (48% versus 34%) and lower population of no invasion (i) (19% vs 26%) for 9 and 6 J cm^{-2}, respectively, might indicate more efficient force exertion for more viscous 9 J cm^{-2} IPLM, as discussed in the earlier work on supported lipid membranes.[7] This tendency also agreed with the slight shape changes of the photobleached region at 6 J cm^{-2} in the FRAP measurement (Figure S3, Supporting Information). However, further analysis of the actin retrograde flow speed on the two interfaces are needed to attribute the small difference in these populations.

The single-cell population density of cellular adhesion phenotypes is correlated with the mechanical properties of IPLM, revealing unanticipated relationships between cell type and IPLM viscoelasticity. Although invasion serves as an important determinant of adhesion, cellular adaptive wetting revealed the interplay between cells and the deformation of IPLM. This raises the question of what other shape parameters are coupled with IPLM viscoelasticity and how the interplay can be understood quantitatively. Here, we relate cellular dimension and invasion depth to the IPLM viscoelasticity changes. The quantification of cellular dimension and invasion depth can be directly read out from the above four cellular phenotypes to understand the correlation between cellular adaptive wetting and morphology changes. Figure 5d,e summarizes IPLM deformation (Figure 5d) and cellular dimension (Figure 5e) at the cellular deepest invasion states. Both interfacial deformation and cellular dimension exhibited a biphasic response. At low crosslinking levels with 3 J cm^{-2} irradiation, the invasion depth was small (≈1.8 µm). It seems reasonable that the cells were not able to build up contractile forces owing to force dissipation,[7] considering the lateral mobility of the IPLM characterized by the FRAP measurement. However, by increasing the viscosity to that of the IPLM with 6 and 9 J cm^{-2} irradiation, there were no significant differences at the deep invasion depth of ≈21 µm. By proceeding with UV irradiation, the IPLM with strong stiffness presented higher resistance against the cellular traction force, which resulted in partial invasion of cells of ≈12 µm. Therefore, the corresponding cellular adhesion changed by manipulating the interfacial viscoelasticity. Cellular dimension also showed a similar tendency (Figure 5e). Especially for intermediated crosslinking levels at 6 and 9 J cm^{-2}, cells exhibited significantly elongated dimensions (≈34 µm) compared

© 2025 The Author(s). Advanced Functional Materials published by Wiley-VCH GmbH

16163028, 0, Downloaded from https://advanced.onlinelibrary.wiley.com/doi/10.1002/adfm.202414534 by Cochrane Japan, Wiley Online Library on [16/01/2025]. See the Terms and Conditions (https://onlinelibrary.wiley.com/terms-and-conditions) on Wiley Online Library for rules of use; OA articles are governed by the applicable Creative Commons License

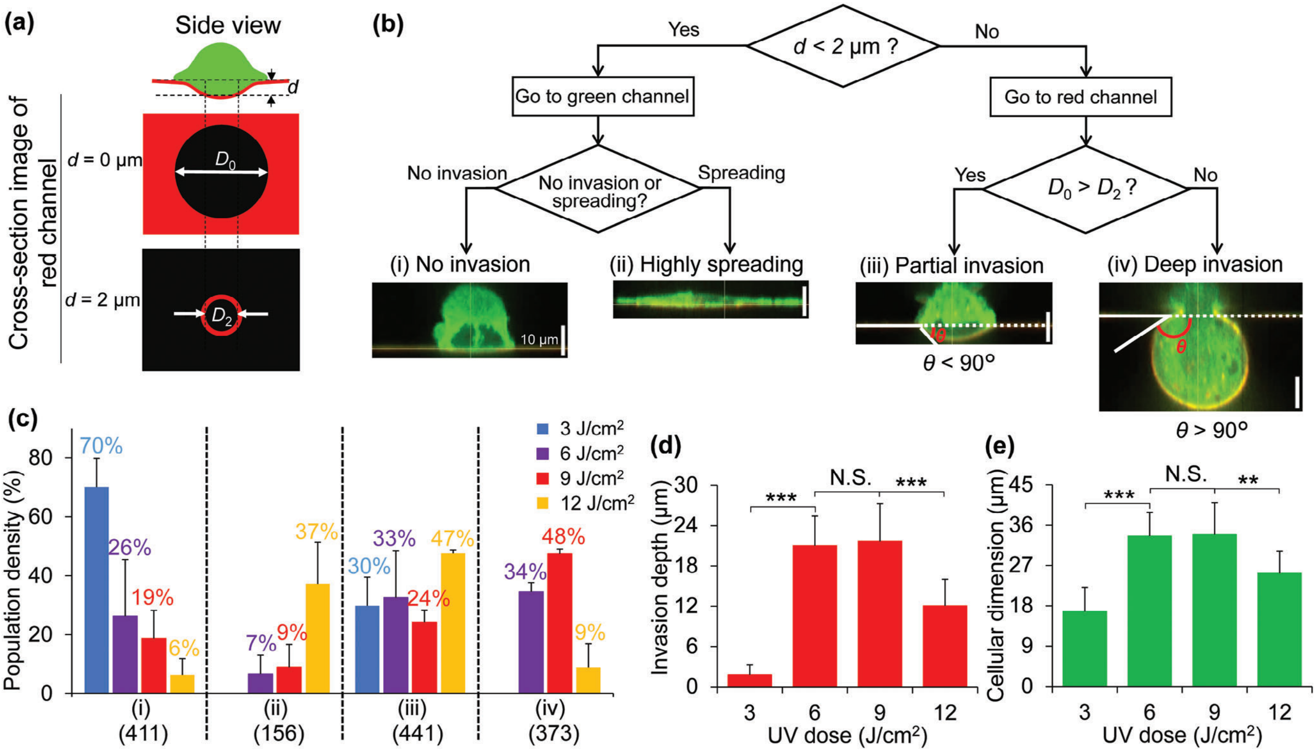

Figure 5. Quantification of the impact of IPLM viscoelasticity on cellular wetting behaviors for single-cell populations. a) Schemes used for classification of cellular adhesion states. The reconstituted side view was used to determine the IPLM indentation depth (*d*) and the cellular morphology either from red and green fluorescence channels, or both. The cross-section views of the red fluorescent channel at $d = 0$ and 2 µm were used to detect the convergent boundary between cell and IPLM, whose diameter was defined as D_0 and D_2, respectively. b) Flow chart of the image processing strategy. By considering of the values of *d*, D_0, D_2, and cellular morphology, the cell adhesive phenotypes on the IPLM were classified into four groups. If the invasion depth was smaller than 2 µm, cells were divided into (i) no invasion or (ii) highly spreading by processing the green fluorescence channel. If the invasion depth was higher than 2 µm, they were further divided into another two groups by comparing D_0 and D_2: (iii) partial invasion and (iv) deep invasion. Representative images are shown at the bottom. θ represents cellular incident angle in the PFCL phase. c) Distribution percentage of cellular phenotypes with regard to the UV irradiation dose. The number of analyzed cells is indicated in parentheses below each bar. d,e) Quantification of changes in adhesion parameters: (d) invasion depth and (e) cellular dimension. The number of analyzed cells is 21, 20, 25, and 6, for 3, 6, 9, and 12 J cm^{-2}, respectively. Statistical differences were analyzed using Student's *t*-test: $^{*}p < 0.05$, $^{**}p < 0.01$, and $^{***}p < 0.001$. N.S., no significance, $p \geq 0.05$.

with those of 3 and 12 J cm^{-2}, presumably owing to the elastic resistance forces of the IPLM squeezing the cell body into the upper aqueous layer.[11] Although the depth and cellular dimension were no different at either 6 or 9 J cm^{-2} owing to the cellular dimension limitation, the stiffer one may provide higher resistance force by improving the efficiency of forces transmission.

3. Discussion

Our study demonstrates the application of a new photopolymerizable IPLM as a cell scaffold, which displays tunable mechanical properties and thereby enables the study of dynamic adhesion behavior changes in cells together with the IPLM in response to the altered viscoelastic properties of a model ECM. Although our previous work reported the physically mixed phospholipid interface,[11] in which the lower phase of the hydrophobic species needs to be changed to adjust the interfacial tension to investigate the adhesion behavior, our current approach enabled controlling the degree of crosslinking by UV shining to tune viscosity and elasticity. Specifically, this platform allows us to fabricate ECM mimics, where the viscosity balance between cell and ECM can be manipulated, to build fundamental knowledge about the influence of dynamic viscoelasticity of both cells and ECM on the adaptive wetting behavior.

The viscosity-tunable nature of the new IPLM was investigated using FRAP by measuring the lateral diffusion of fluorescent-labeled phospholipids. At lower irradiation doses, fluidity was observed owing to the recovery of the bleached region. With increasing irradiation dose up to 6 J cm^{-2}, the lateral fluidity was significantly suppressed. However, this did not mean the completion of the crosslinking reaction above 6 J cm^{-2}, rather it continued to change the viscoelastic nature with prolonged irradiation verified by interfacial rheology. Interfacial elasticity was characterized by nanoindentation using AFM, with a significant decrease in the out-of-plane deformability above 9 J cm^{-2}. Further dismantling the interfacial apparent modulus into material modulus and interfacial tension-derived pre-stress, the mechanical maturation of the IPLM was demonstrated, with a transition from the interfacial tension-dominating state to the materials modulus-dominating one in response to increasing crosslinking levels. Therefore, the successful preparation of a highly deformable fluid interface with varying viscoelasticity was confirmed.

© 2025 The Author(s). Advanced Functional Materials published by Wiley-VCH GmbH

16163028, 0, Downloaded from https://advanced.onlinelibrary.wiley.com/doi/10.1002/adfm.202414534 by Cochrane Japan, Wiley Online Library on [16/01/2025]. See the Terms and Conditions (https://onlinelibrary.wiley.com/terms-and-conditions) on Wiley Online Library for rules of use; OA articles are governed by the applicable Creative Commons License

By observing epithelial MDCK cells seeded on the IPLM using confocal microscopy, we found that the cells actively deformed the fluid interface by switching the dimensions of the IPLM from a 2D- to a 3D-like structure to reshape the adhesive environment over time. To date, the impact of viscoelasticity on cellular adhesion behaviors has been discussed on viscoelastic hydrogels or viscous-supported lipid bilayers. The viscous nature is introduced into either the materials' bulk or interface, and its impact on the cellular straightforward transition from spherical morphology to the spreading state is established via molecular clutch-based adhesions in a similar fashion to that of the elastic component. In contrast to this so-called canonical wetting behavior, we are able to see the viscoelastic regulation of cellular adaptive wetting in terms of the degree of out-of-plane deformation depending on the balance between cellular and IPLM viscosity in our highly deformable viscoelastic platform. In our previous report,[11] we have experimentally simulated cellular adaptive wetting behaviors using viscous PDMS drops at the air-water interface. We found that adaptive wetting emerged only by matching the timescale of viscous relaxation of the PDMS drops and the observation timescale. By increasing the PDMS viscosity, the indentation of the PDMS-water interface become larger with a smaller deformation of the PDMS drop. Considering these previous simulation results, the cellular viscosity increase/decrease is expected to result in an increase/decrease in cellular invasion depth and retardation/acceleration of the cellular spreading process in our system. Moreover, we also observed that the interface with medium viscoelasticity or stiffness allowed significant diving of the cells into the PFCL with increasing cellular dimension, which is significantly different from cell adhesion behaviors on conventional viscoelastic platforms. This biphasic profile was reminiscent of an earlier work in which the intermediate viscosity of soft substrate regulated optimal cellular spreading speed,[1] emphasizing the importance of viscosity-based regulation.

From an application perspective, this new viscoelastically-tunable IPLM could be further used to engineer cellular fate, as the platform is capable of manipulating cellular adaptive wetting, where mechanical forces are dynamic depending on the degree of out-of-plane deformation. During cellular deep invasion, the IPLM switches from a 2D planar surface to a quasi-3D form by wrapping the cell body, thereby enabling the cells to receive biochemical and mechanical cues from the majority of the surface without undergoing significant morphological alterations. This configuration, featuring a 3D contacting area between cells and the model ECM, closely resembles native tissues. In contrast, conventional 2D substrates require cells to be flattened to maximize their interactions with ECMs. Subsequent reversible deformations modulate the rearrangement of the cytoskeleton. By considering the existence of cellular mechanical hysteresis,[32] where cellular functions and fate are regulated not only by the mechanics of their surrounding environment at that moment, but also by those to which the cells have been exposed in the past, the dynamic changes in IPLM mechanics can impact single cell functions, like the speed of actin retrograde flow and stem cell fate decision. The cell traction force-driven 3D cellular environments described above might be advantageous over the usual 3D culture platform in terms of precise optical imaging and cell harvesting. This allows the target cells to be addressable both microscopically and enzymatically at the 2D fluid interface, thereby enabling direct correlation of microscopic analysis data and gene expression patterns after trypsinization. This will be useful to further investigate how cell-matrix bidirectional interaction regulates cellular activities. Consequently, we hypothesize that our method can facilitate the precise control of cell–matrix interactions at the single-cell level, which may enable the prediction of dynamic cellular responses in physiological and pathological processes, such as immune cell extravasation and EMT in cancer progression.

4. Conclusion

This study reports a new photopolymerizable fluid interfacial cellular scaffold, displaying tunable viscoelastic properties depending on the crosslinking level. Our system offers a systematically manipulable viscoelasticity platform that can reveal the impact of material viscoelastic properties on cellular adhesion behaviors, specifically cellular adaptive wetting, with different degrees of out-of-plane deformation; this cannot be observed in conventional solid- or hydrogel-based materials. These adaptive wetting transitions depending on the balance between cellular and IPLM viscosity may enable the prediction of dynamic adhesion responses in physiological and pathological processes. Furthermore, our new viscoelasticity-tunable interface can be used to engineer cellular fate, as the platform is capable of mechanobiologically manipulating cellular 2D-to-3D transition behaviors, where mechanical forces between the cell and model ECM change dynamically both in time and space.

The apparent modulus of IPLM (up to 10 kPa for 12 J cm^{-2}) can cover the range of softer living tissues, such as brain[2] and bone marrow.[33] Moreover, our IPLM platform shows mechanics with stronger modulus in the in-plane direction but smaller value for the out-of-plane direction. We can find similar mechanical anisotropy[34] in living tissues, including the brain tissue, cornea,[35] endothelial layer in the blood vessels,[36] and the bone marrow niche.[33] Therefore, cellular behaviors in our model system could mimic cellular mechanical responses in in vivo environments.

During cellular adaptive wetting, cells undergo dynamic dimensional changes. These share similarities to the EMT process and extravasation of immune cells. As an epithelial cell type, MDCK cells can transit from a spherical shape with a collective feature to single cells with spreading morphology via the EMT-like process. Through this, the cells undergo a dynamic change in dimension, losing the cohesive nature and increasing mobility. This phenomenon can be a hallmark of epithelial cancer cells undergoing invasion and metastasis.[37] Another example is the inflammation-induced emigration of immune cells from the bloodstream into the tissue. The immune cells undergo a morphological change from a circular to an amoeboid shape to adhere to the inflamed endothelium to identify an entry point. This process eventually results in their extravasation into the infected tissue. This transition is accompanied by a substantial alteration in dimensional parameters.[38] The similarity between cellular dimensional changes at the interface and these in vivo events makes our system a promising tool for studying dynamic cell behavior and interactions in physiological environments. This advancement has the potential to enable more precise predictions of cellular responses in real-life biological processes.

© 2025 The Author(s). Advanced Functional Materials published by Wiley-VCH GmbH

16163028, 0, Downloaded from https://advanced.onlinelibrary.wiley.com/doi/10.1002/adfm.202414534 by Cochrane Japan, Wiley Online Library on [16/01/2025]. See the Terms and Conditions (https://onlinelibrary.wiley.com/terms-and-conditions) on Wiley Online Library for rules of use; OA articles are governed by the applicable Creative Commons License

5. Experimental Section

Reagents: The 1,2-bis(10,12-tricosadiynoyl)-sn-glycero-3-phosphocholine (DA–PC), 1,2-Distearoyl-sn-glycero-3-phosphocholine (18:0 PC, DSPC), 1,2-distearoyl-sn-glycero-3-phosphoethanolamine-N-[4-(p-(cysarginylglycylaspartate-maleimidomethyl)cyclohexane-carboxamide] (RGD-DSPE), and 1,2-dioleoyl-sn-glycero-3-phosphoethanolamine-N-(lissamine rhodamine B sulfonyl) (Liss-Rhod DOPE) were purchased from Avanti polar lipids (Alabaster, AL, USA). FC-70, trichloro(3,3,4,4,5,5,6,6,7,7,8,8,8-tridecafluorooctyl) silane, fluorescein isothiocyanate labeled bovine serum albumin (FITC-BSA), and transforming growth factor (TGF)-β_1 were obtained from SIGMA-Aldrich (St. Louis, MO, USA). Potassium hydroxide (KOH), chloroform, ethanol, and phosphate buffered saline (PBS) tablets were purchased from Wako (Tokyo, Japan).

Unilamellar Vesicle Preparation: Solid DA–PC, DSPC, RGD-DSPE, and Liss-Rhod DOPE at a ratio 85/12.5/2/0.5 mol.% was dissolved in chloroform as a stock solution and stored at −20 °C until use. A lipid film in a 10 mL glass vial was formed by evaporating the chloroform in the mixed stock solution and then drying the lipids under vacuum for ≈3 h. The mixed lipid film was hydrated in PBS to a final concentration of 1 mᴍ. The suspension was heated to 50 °C in an oven with manual shaking from time to time. Immediately after heating, the lipid suspension was sonicated for clarity at RT using a probe-type ultrasonic disrupter (UD-100; Tomy, Tokyo, Japan) with 10 cycles of intermittent operation (45 s high-power sonication separated by 30 s intervals). Then, the smaller lipid vesicles were sized by 21 extrusion cycles through a 0.1 µm polycarbonate membrane in a Mini-Extruder (Avanti Polar Lipids, Alabaster, AL, USA). The temperature of the sample and extruder was maintained at > 43 °C with a heater. Subsequently, the lipid suspension was held in a 50 °C oven until further processing.

Assembling the IPLM Platform: Fluorination of the in-house-developed cell culture chamber (inner wall: 21 mm; outer wall: 25 mm) was performed as previously described.[11] Chambers were activated with potassium hydroxide (KOH, 10 wt.%) at 60 °C for 1 h, then rinsed with deionized water and dried under air flow. The bottom glass was then fluorinated by trichloro(3,3,4,4,5,5,6,6,7,7,8,8,8-tridecafluorooctyl) silane (0.5 vol.%) in ethanol solution followed by a 30-min heating process at 70 °C. It was then rinsed 2–3 times with ethanol and water for glass cleaning and sterilized by autoclaving.

To form the water-perfluorocarbon interface, the above fluorination allowed the FC-70 (250 µL) wetting well at the lower layer, followed by 2 mL PBS. Next, the preheated phospholipid vesicle solution was added to the upper layer of the PBS to reach a final phospholipid concentration of 0.2 mᴍ. The IPLM assembly process was carried out at RT for 2 h. After successful IPLM layer formation, the membranes were slowly washed by repeatedly replacing the upper layer with fresh PBS before lowering the temperature to 0 °C with ice. The system was cooled to ≈0 °C to produce the oriented reactive DA–PC monomer, avoid the thermal hysteresis, and make the DA–PC light sensitive after warming above its phase transition temperature.[39] Then, the cooled IPLM was allowed to warm to RT for 35 min to equilibrate and promote the growth of the DA–PC-rich domains before UV-initiated polymerization, because the fluid lipid phase would promote the incorporation of DA–PC-rich domains.[23] Photosensitivity was retained even if the membranes were warmed to RT after cooling to ≈0 °C.

254 nm UV Irradiation: The equilibrated IPLM was exposed to 254 nm UV light at RT (CL-1000 Ultraviolet Crosslinker, USA; short-wave assembly 115 V, 60 Hz, and 254 nm) and a distance of 5 cm from the lamp. The UV irradiation dose was adjusted by varying the exposure time. For each irradiation cycle, a UV light dose of 1 J cm^{-2} was used with different numbers of irradiation cycles (3, 6, 9, and 12 cycles, with ≈2.5 min per cycle).

Upon irradiation of the unilamellar vesicles, aqueous dispersion was conducted with 254 nm UV light (prior to UV irradiation, vesicles were already lowered to near 0 °C, then equilibrated to RT). The appearance of the dispersion color was associated with the polymerization reaction of DA–PC within the liposome.

UV–Vis Spectroscopy: Wavelength-dependent absorbance spectra of the unilamellar vesicles were obtained using a UV–vis spectrophotometer (UV-Vis; UV-2600, Shimadzu, Kyoto, Japan) at RT. UV (365 nm and 10 mW cm^{-2}) or vis (436 nm and 9 mW cm^{-2}) light was irradiated from the top using a mercury lamp (SX-UI 251HQ, USHIO, Tokyo, Japan). The wavelength of irradiated light was selected using bandpass filters (Edmund Optics). The polymerization reaction was monitored in the wavelength range between 350 and 650 nm.

Ligand Mobility Test of the IPLM: FRAP was used to measure the extent of lateral ligand mobility within the IPLM using a BX-51 upright fluorescence microscope (Olympus) equipped with a 60× water-immersion objective lens (Olympus, LUMPlanFLN, Rochester, USA) and CMOS camera (MD-695, Molecular Devices, San José, CA, USA) operated using the MetaMorph software (MetaMorph Inc., Nashville, TN 37212). A defined polygonal region was selected as an ROI for photobleaching by photoirradiation with 545 ± 5 nm light for 3 min at a polygonal region. Fluorescence images of the IPLM were obtained after a given time interval.

Interfacial Rheology: The rheology of IPLM at the liquid–liquid interface was measured using a rheometer (Discovery HR-20, TA Instruments) with double wall ring (DWR) geometry equipped with a Delrin trough with a circular channel. Briefly, FC-70 (19 mL) was added to the Delrin trough. Excess FC-70 solvent was removed to the level of the liquid layer close to the sidewall step. A lipid suspension (0.2 mᴍ and 20 mL) was carefully added on top of the FC-70 layer. After the above same IPLM assembling process (Section Assembling the IPLM Platform) and UV irradiation (Section 254 nm UV Irradiation), the DWR was lowered to pass through the aqueous layer until its contact with the FC-70 liquid layer by monitoring the axial force, followed by further lowering by 500 µm. Frequency sweeps were performed with a constant displacement of 1.0×10^{-3} rad at 25 °C.

Atomic Force Microscopy (AFM): AFM was performed to image the in situ planar IPLM using a Nanowizard 4 (JPK BioAFM, Bruker Nano GmbH, Berlin, Germany). A gold-coated silicon nitride AFM cantilever (Novascan Technologies, Ames, IA, USA) and SiO_2 particles with a radius of 300 nm and a spring constant of 0.06 N m^{-1} were used.

After the system was well calibrated, AFM imaging was performed at RT (≈25 °C). All images were recorded at a resolution of 64 × 64 pixels. The force and scanning speed were optimized to minimize damage. Images were analyzed and processed using the JPKSPM software (JPK/Bruker, Berlin, version 8.0.111).

Further curve fitting based on the Hertz model was used rather than the value from the stiffness map because the measured response should represent the material deformation only. An explanation for this discrepancy could be the influence of the distortion of the cantilever during the indenting process.

For dismantling the AFM analysis into the interfacial tension at the fluid interface (pre-stress) and the IPLM crosslinking-derived modulus, according to the previous report,[28] the prestress and modulus were fitted using Equation (1) at the total 16 positions by focusing on the deformation range at 100 nm after removing the cantilever distortion. Fitting errors at each indentation were also calculated to optimize the best prestress and modulus.

$$F = 4\pi R d \sigma \cos[\tan^{-1}(2\sqrt{\frac{R}{d}})] + \frac{4}{3\left(1-\gamma^2\right)} E \sqrt{R} d^{1.5} \tag{1}$$

R: tip radius; σ: pre-stress; d: deformation; γ: Poisson's ratio; E: modulus.

Protein Adsorption Test on IPLM: A mixed protein solution of FITC–BSA and regular BSA at a weight ratio of 1:9 to a final concentration 0.5 mg mL^{-1} acted as the fouling agent for fluxing the IPLM. After incubation at 37 °C for 1 h, the protein was removed by repeatedly replacing the PBS in the upper layer with fresh PBS. The water–PFCL interface without phospholipid assembly served as a pristine interface; the test results are shown in Figure S8 (Supporting Information).

Cell Viability Assessment: Live/dead cell staining kit (Invitrogen) was employed to assess the viability of non-transfected MDCK cells (thereby no fluorescence from the lifeact-GFP) on the IPLM after incubation for 2–3 h. The staining solution was prepared by mixing 5 µL of Calcein-AM and 20 µL ethidium homodimer into 10 mL culture medium. After seeding cells on each IPLM case for 2 h, upper medium was replaced by the above

© 2025 The Author(s). Advanced Functional Materials published by Wiley-VCH GmbH

16163028, 0, Downloaded from https://advanced.onlinelibrary.wiley.com/doi/10.1002/adfm.202414534 by Cochrane Japan, Wiley Online Library on [16/01/2025]. See the Terms and Conditions (https://onlinelibrary.wiley.com/terms-and-conditions) on Wiley Online Library for rules of use; OA articles are governed by the applicable Creative Commons License

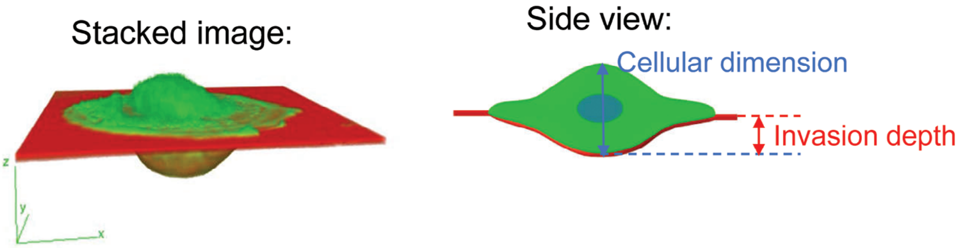

Scheme 1. Reconstructed 3D stacked image of IPLM together with a single cell. The right shows a side view of the 3D reconstruction. The quantification of cellular dimension and invasion depth can be directly read from the side view.

medium containing the dye. Then the image of cells on the IPLM with different crosslinking level was captured and quantified by using ImageJ software.

Cell Culture with IPLM: The culture medium for Madin-Darby Canine Kidney (MDCK) cells (RCB0995, RIKEN cell bank) that stably expressed lifeact-GFP was prepared by diluting 10× minimal essential medium (MEM, Thermo Fischer Scientific, Waltham, Massachusetts, U.S.) 10 times, and supplementing it with 10% heat-inactivated fetal bovine serum (FBS, EU origin, Biowest, Naullie, France), 100 units mL^{-1} penicillin, 100 mg mL^{-1} streptomycin (Nacalai, Kyoto, Japan), 1% MEM-nonessential amino acids (Nacalai), 1% sodium pyruvate (Nacalai), 1% L-glutamate (Nacalai), and 2.2 g L^{-1} sodium hydrogen carbonate (Wako). The cells were cultured in a Petri dish by adding 10 ng mL^{-1} TGF-β_1 to the above culture medium for 24 h at 37 °C, supplemented with 5% CO_2. Before seeding the cells onto the IPLM, the upper aqueous phase (PBS) of the as-fabricated IPLM platform was replaced with the cell culture medium. For seeding cells to the IPLM platform, the lifeact-GFP-expressing MDCK cells were harvested from the culture dish using trypsin-ethylenediamine tetraacetic acid (Wako) and plated onto the IPLM platform at a density of 2×10^4 cells cm^{-2} and incubated at 37 °C with 5% CO_2 for ≈1–2 h before observation.

Imaging by Confocal Microscopy: CLSM images were obtained using an inverted microscope (IX-81; Olympus, Shinjuku, Japan) equipped with a disc-scan confocal unit CSU10 (Yokogawa, Tokyo, Japan), an Andor laser combiner (Oxford Instruments, Oxfordshire, UK), an MD-695 CMOS camera, and a 60× water immersion lens (LUMPlanFL N; Olympus) to observe the cells on the IPLM from the bottom of the chamber with a humidified 37 °C incubator supplemented with 5% CO_2. The observation could be obtained through two channels: the red channel is the IPLM with a fluorescence tag and the green channel is actin cytoskeleton of MDCK cells. The stacked 3D images of a cell together with the IPLM were built by reconstructing the z-axis sequenced scans at the desired thickness step (0.5 or 2 µm). By employing orthogonal analysis with the Fiji software, the top views and side views could be directly read from the stacked images.

Cell and IPLM Morphological and Invasion Depth Analysis: The invasion depth/IPLM deformation and cellular morphology change were analyzed using the Fiji software. As illustrated in **Scheme 1**, by merging the confocal images of the green (cell) and red (IPLM) channels, the stacked 3D structures for both the cell and IPLM were reconstructed at a 0.5 µm thickness of each cross-sectional image. The side view was obtained through orthogonal processing. Then, the cellular dimensions and invasion depth could be directly read using the side-view image of the stacked 3D structures.

Statistical Analysis: Statistical analyses for the two groups were performed using a Student's *t*-test for the technical replicates indicated in each figure. All error bars represent standard deviations. Statistical analyses were performed using Microsoft EXCEL.

Supporting Information

Supporting Information is available from the Wiley Online Library or from the author.

Acknowledgements

This study was supported in part by the Japan Society for the Promotion of Science, KAKENHI (22H00596 and 23K17481 to J.N.: 23KJ2167 to H.W.).

Conflict of Interest

The authors declare no conflict of interest.

Data Availability Statement

The data that support the findings of this study are available from the corresponding author upon reasonable request.

Keywords

adaptive wetting, adhesion, biphasic, crosslinking, extracellular matrix

Received: August 9, 2024
Revised: December 30, 2024
Published online:

[1] Z. Gong, S. E. Szczesny, S. R. Caliari, E. E. Charrier, O. Chaudhuri, X. Cao, Y. Lin, R. L. Mauck, P. A. Janmey, J. A. Burdick, V. B. Shenoy, *Proc. Natl. Acad. Sci. U. S. A.* **2018**, *115*, E2686.
[2] A. J. Engler, S. Sen, H. L. Sweeney, D. E. Discher, *Cell* **2006**, *126*, 677.
[3] O. Chaudhuri, J. Cooper-White, P. A. Janmey, D. J. Mooney, V. B. Shenoy, *Nature* **2020**, *584*, 535.
[4] O. Chaudhuri, *Biomater. Sci.* **2017**, *5*, 1480.
[5] O. Chaudhuri, L. Gu, D. Klumpers, M. Darnell, S. A. Bencherif, J. C. Weaver, N. Huebsch, H. P. Lee, E. Lippens, G. N. Duda, D. J. Mooney, *Nat. Mater.* **2016**, *15*, 326.
[6] C. Müller, A. Müller, T. J. S. M. Pompe, *Soft Matter* **2013**, *9*, 6207.
[7] M. Bennett, M. Cantini, J. Reboud, J. M. Cooper, P. Roca-Cusachs, M. Salmeron-Sanchez, *Proc. Natl Acad. Sci. U. S. A.* **2018**, *115*, 1192.
[8] M. Cantini, H. Donnelly, M. J. Dalby, M. Salmeron-Sanchez, *Adv. Healthcare Mater.* **2020**, *9*, 1901259.
[9] B. Sabass, U. S. Schwarz, *J. Phys. Condens. Matter* **2010**, *22*, 194112.
[10] Y. Bu, L. Li, C. Yang, R. Li, J. Wang, *Acta Mech. Solida Sin.* **2019**, *32*, 599.
[11] Z. Lu, M. Tenjimbayashi, J. Zhou, J. Nakanishi, *Adv. Mater.* **2024**, *36*, 2403396.
[12] S. K. Hu, S. W. Hsiao, H. Y. Mao, Y. M. Chen, Y. Chang, L. Chao, *Sci. Technol. Adv. Mater.* **2013**, *14*, 044408.
[13] M. Callens, M. Beltrami, E. D'Agostino, H. Pfeiffer, D. Verellen, G. Paradossi, K. Van Den Abeele, *Coll. Surf. A Physiochem. Eng. Asp.* **2019**, *568*, 371.

© 2025 The Author(s). Advanced Functional Materials published by Wiley-VCH GmbH

16163028, 0, Downloaded from https://advanced.onlinelibrary.wiley.com/doi/10.1002/adfm.202414534 by Cochrane Japan, Wiley Online Library on [16/01/2025]. See the Terms and Conditions (https://onlinelibrary.wiley.com/terms-and-conditions) on Wiley Online Library for rules of use; OA articles are governed by the applicable Creative Commons License

[14] C. F. Temprana, E. L. Duarte, M. C. M. Taira, M. T. Lamy, S. del Valle Alonso, *Langmuir* **2010**, *26*, 10084.
[15] S. Baek, M. Dinh Phan, J. Lee, K. Shin, *Polym. J.* **2016**, *48*, 457.
[16] A. Puri, H. Jang, A. Yavlovich, M. A. Masood, T. D. Veenstra, C. Luna, H. Aranda-Espinoza, R. Nussinov, R. Blumenthal, *Langmuir* **2011**, *27*, 15120.
[17] S. Alonso-Romanowski, N. S. Chiaramoni, V. S. Lioy, R. A. Gargini, L. I. Viera, M. C. Taira, *Chem. Phys. Lipids* **2003**, *122*, 191.
[18] J. J. Schaefer, C. B. Fox, J. M. Harris, *J. Raman Spectrosc.* **2012**, *43*, 351.
[19] B. M. Peek, J. H. Callahan, K. Namboodiri, A. Singh, B. P. Gaber, *Macromolecules* **1994**, *27*, 292.
[20] T. K. Lind, M. Cárdenas, H. P. Wacklin, *Langmuir* **2014**, *30*, 7259.
[21] T. Okazaki, T. Inaba, Y. Tatsu, R. Tero, T. Urisu, K. Morigaki, *Langmuir* **2009**, *25*, 345.
[22] N. M. Fonseka, B. Liang, K. S. Orosz, I. W. Jones, H. K. Hall Jr, H. S. Christie, C. A. Aspinwall, S. S. Saavedra, *Langmuir* **2019**, *35*, 12483.
[23] K. Okuno, D. Saeki, H. Matsuyama, *Biochim. Biophys. Acta - Biomembr.* **2020**, *1862*, 183377.
[24] L. Costa, G. Li-Destri, D. Pontoni, O. Konovalov, N. H. Thomson, *Adv. Mater. Interfaces* **2017**, *4*, 1700203.
[25] G. Espinosa, I. L. López-Montero, F. Monroy, D. Langevin, *Proc. Natl Acad. Sci. U. S. A.* **2011**, *108*, 6008.
[26] R. Masrat, M. Maswal, O. A. Chat, G. M. Rather, A. A. Dar, *Colloids Surf. A: Physicochem. Eng. Asp.* **2016**, *489*, 113.
[27] W. Megone, D. Kong, L. Peng, J. E. Gautrot, *J. Colloid. Interface Sci.* **2021**, *594*, 650.
[28] H. Wang, H. Zhang, R. Tamura, B. Da, S. A. Abdellatef, I. Watanabe, N. Ishida, D. Fujita, N. Hanagata, T. Nakagawa, J. Nakanishi, *Sci. Technol. Adv. Mater.* **2023**, *24*, 2265434.
[29] W. R. Legant, C. K. Choi, J. S. Miller, L. Shao, L. Gao, E. Betzig, C. S. Chen, *Proc. Natl Acad. Sci. U. S. A.* **2013**, *110*, 881,
[30] B. A. Nerger, M. J. Siedlik, C. M. Nelson, *Cell. Mol. Life Sci.* **2017**, *74*, 1819.
[31] S. S. Hur, Y. Zhao, Y. S. Li, E. Botvinick, S. Chien, *Cell. Mol. Bioeng.* **2009**, *2*, 425.
[32] L. Yu, Y. Hou, W. Xie, J. L. Cuellar-Camacho, Q. Wei, R. Haag, *Adv. Mater.* **2020**, *32*, 2006986.
[33] L. E. Jansen, N. P. Birch, J. D. Schiffman, A. J. Crosby, S. R. Peyton, *J. Mech. Behav. Biomed. Mater.* **2015**, *50*, 299.
[34] D. Kong, W. Megone, K. D. Q. Nguyen, S. Di Cio, M. Ramstedt, J. E. Gautrot, *Nano Lett.* **2018**, *18*, 8811946.
[35] N. Khuu, S. Kheiri, E. Kumacheva, *Trends Chem.* **2021**, *3*, 1002.
[36] P. L. Ko, C. K. Wang, H. H. Hsu, T. A. Lee, Y. C. Tung, *Acta Biomater.* **2022**, *145*, 316.
[37] S. Yamamoto, T. Miyama, T. Komoda, M. Sugawara, M. Nonomura, J. Nakanishi, *Anal. Sci.* **2020**, *36*, 263.
[38] M. Schnoor, E. Vadillo, I. M. Guerrero-Fonseca, *Curr. Opin. Physiol.* **2021**, *19*, 119.
[39] D. F. O'Brien, T. H. Whitesides, R. T. Klingbiel, *J. Polym. Sci. Polym. Lett. Ed.* **1981**, *19*, 95.

© 2025 The Author(s). Advanced Functional Materials published by Wiley-VCH GmbH

16163028, 0, Downloaded from https://advanced.onlinelibrary.wiley.com/doi/10.1002/adfm.202414534 by Cochrane Japan, Wiley Online Library on [16/01/2025]. See the Terms and Conditions (https://onlinelibrary.wiley.com/terms-and-conditions) on Wiley Online Library for rules of use; OA articles are governed by the applicable Creative Commons License